Journal of Materials Chemistry A

ROYAL SOCIETY OF CHEMISTRY

PAPER

View Article Online
View Journal | View Issue

Cite this: J. Mater. Chem. A, 2025, 13, 13126

High surface area mesoporous carbon nanodendrites – detonation synthesis, characterization and use as a novel electrocatalyst support material†

Thomas Merzdorf, ‡[a] An Guo, ‡[a] Pierre Schröer, [a] Elisabeth Hornberger, [a] Sebastian Ott,[a] Laurin Riebel,[a] Jessica Hübner,[a] Liang Liang,[a] Malte Klingenhof,[a] Matthias Kroschel,[a] Marleen Hußmann, [b] Siegfried Eigler, [b] Alisa Kozhushner,[c] Lior Elbaz [c] and Peter Strasser *[a]

Received 25th October 2024
Accepted 20th March 2025

DOI: 10.1039/d4ta07621d

rsc.li/materials-a

Carbon supports play a crucial role in the performance and durability of the proton exchange membrane fuel cell (PEMFC). The porosity of carbon particles and the carbon matrix, as well as the surface area, is essential for good transport of oxygen, water and electrons. In this work, the synthesis and characterization of extremely high surface-area, mesoporous carbon nanodendrites (MCNDs) formed by controlled detonation are presented. This new carbon material is used as a cathode catalyst's support material in PEMFCs. Annealed at three different temperatures and compared to commercial carbon supports, the graphitization and ordering degree of the carbons are investigated. Pt nanoparticles are deposited on all support materials using a novel fluidized bed reduction reactor. MCND-based Pt nanoparticle fuel cell cathodes significantly outperform Pt catalysts on commercial carbons in single cell tests in PEMFCs. Online carbon degradation quantification reveals that, due to its unique porous structure and high surface area, corrosive high anodic cell potential cycling leads to pore collapse and hence should be avoided for this kind of support material. This behavior is reduced with higher annealing temperatures.

Introduction

Proton exchange membrane fuel cells (PEMFCs) have attracted significant attention in the last few decades as promising power generators mainly for transportation applications.[1,2] Platinum based catalysts for PEMFCs have been loaded onto support materials to improve their utilization through an increase in their electrochemical surface area (ECSA) and thus reduce platinum group metal (PGM) loadings and the derived cost of PEMFCs.[3–6] Due to their high surface area, electron conductivity, and low production costs, carbon nanoparticles are the most commonly used catalysts' support material.[7] Hence, carbonaceous materials have been of major importance and thus a research focus for various electrochemical applications.[8] The diversity in their physical and chemical properties, as well as their macro- and micro-structure, and morphology, can be tuned depending on the synthesis or post-treatment and allows tailoring the support for their end-use.[9–12]

In the past few decades, researchers have dedicated their efforts to modifying carbon and fine-tuning its properties to suit their specific requirements. For instance, the surface area and the pore structure play a determining role in catalytic applications. For fuel cell operation, the overall performance is predominantly governed by oxygen mass transport on the cathode, indicating that the rate of conversion is more reliant on the quantity of oxygen reaching platinum-based oxygen reduction reaction (ORR) catalytic active sites rather than on its intrinsic activity. Thus, to improve the oxygen transport through the catalyst layer different approaches are reported in the literature.[5] Depending on the surface area, carbon materials are divided into two categories, solid and porous carbons. Solid carbons, such as Vulcan, have moderate surface areas and smaller amounts of pores leading to good mass transport properties, because the catalyst particles are placed on the outside of the carbon support, whereas porous carbons, such as Ketjenblack, exhibit very high surface areas above 500 $m^2\ g^{-1}$; thus, the catalyst particles can be deposited into the pore system of the support material, protecting the nanoparticles from ionomer poisoning.[13] This is achieved using a higher porosity of

[a]Department of Chemistry, Technical University Berlin, 10623 Berlin, Germany. E-mail: pstrasser@tu-berlin.de
[b]Institut für Chemie und Biochemie, Freie Universität Berlin, 14195 Berlin, Germany
[c]Chemistry Department, Bar-Ilan University, 5290002 Ramat-Gan, Israel

† Electronic supplementary information (ESI) available. See DOI: https://doi.org/10.1039/d4ta07621d

‡ T. M. and A. G. contributed equally to this paper.

carbon materials with different fractions of micro- (<2 nm), meso- (2–50 nm) or macropores (>50 nm).[14] Small pores with low tortuosity combine the best of both carbon materials; these "accessible" pores enable good transport and kinetic properties. Yarlagadda *et al.* showed a correlation of the membrane electrode assembly (MEA) performance with the accessibility of Pt nanoparticles inside the carbon pores, displaying improved performance with accessible pores in the range of 4–7 nm.[15] In our recent publication, we presented a similar tendency revealing an improvement in performance with the pore openings of the carbons' internal pore structure.[16] Thus, a mesopore structured high surface area carbon support enables an improved mass activity alongside sufficient oxygen mass transport enhancing performance even at high current densities. Structurally well-defined morphologies are achievable using a templated-based approach and enable all kinds of nanometric shapes of the carbon matrix *e.g.* as rods,[17] spheres,[18] and honeycombs.[19]

Apart from the morphology, the corrosion resistance of the carbon support can be further enhanced by increasing the graphitization degree. Xue *et al.* significantly improved the stability of catalysts by using carbon black treated at 1800 °C.[20] Although the initial performance was similar to that of untreated carbon samples, the maximum catalytic activity was maintained during high potential cycling. Other examples of graphitized carbon supports include the work of Tang *et al.*, who developed a 3D hierarchical carbon support. Catalysts supported on this carbon exhibited a high ECSA of 106 $m^2\ g^{-1}$ and showed only a 5% decrease in power density during a PEMFC single-cell test after cycling between 0.6 and 1.2 V for 30 000 cycles.[21]

Even though tremendous effort has been made in the research of different carbon materials, there is no generic state-of-the-art carbon for all electrochemical devices as adjustments for the individual requirements are needed. For Pt-based PEMFC catalyst systems, high surface area carbon is predominantly used, due to the beneficial effect of the tailored pore structure on the fuel cell performance.[22–25]

Herein, we report a novel family of mesoporous carbon nanodendrite (MCND) materials synthesized in a one-pot preparation reaction and show its advantages as a support material for Pt nanoparticles in PEMFC electrodes. We analyzed the pore structure using N_2 physisorption and the graphitization of the carbon *via* Raman spectroscopy, deposited Pt nanoparticles on the carbon and investigated the performance and durability of the new carbon support material in a rotating disk electrode (RDE) and MEA measurements in comparison with three commercial carbon support materials: Vulcan (Vulcan XC 72R), KB300 (Ketjenblack EC-300J) and KB600 (Ketjenblack EC-600JD), showing superior performance under operating conditions for MCND-based systems.

Results and discussion

Mesoporous carbon nanodendrite (MCND) powder materials were obtained using a one-pot synthesis with subsequent detonation in a stainless-steel reactor (see Fig. S1†). In aqueous solution, dissolved $AgNO_3$ reacts with acetylene (C_2H_2) gas to form a very unstable Ag_2C_2 salt. To avoid the generation of unwanted silver salts, the reaction is conducted in ammonia solution to buffer the created NO_3^- anion in the form of ammonium nitrate (eqn (1)). Consequently, the reaction favors the generation of pure Ag_2C_2 which will then decompose to elemental silver and pure carbon (eqn (2)).

$$2AgNO_3 + C_2H_2 + NH_{3(aq.)} \rightarrow Ag_2C_2 + 2NH_4NO_3 \quad (1)$$

$$Ag_2C_2 \rightarrow 2Ag + 2C \quad (2)$$

The synthesis yielded nano-scaled carbon dendrites, Fig. 1d–f. In order and stabilize the carbon while maintaining the

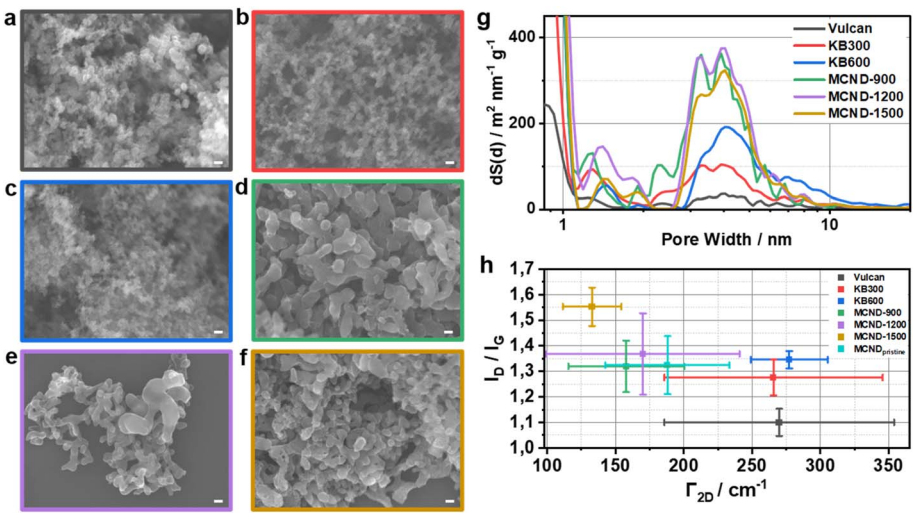

Fig. 1 SEM images at 50k magnification of (a) Vulcan (black), (b) KB300 (red), (c) KB600 (blue), (d) MCND-900 (green), (e) MCND-1200 (purple), and (f) MCND-1500 (gold); the scale bar represents 100 nm; (g) pore size distribution by QSDFT (quenched solid density functional theory) of N_2 physisorption (N_2 carbon adsorption branch kernel at 77 K for slit/cylindrical pores); (h) statistical Raman spectroscopy (SRS) spectra of all six samples and pristine MCNDs (unannealed, turquoise).

mesoporous structure, a post-synthesis heat treatment of the pristine MCND material was conducted in an Ar atmosphere. Three MCND batches were prepared at varying temperatures and heat treated for 12 h to 900 °C, 1200 °C and 1500 °C, which are denoted as MCND-*X*, where *X* refers to the annealing temperature.

Electron microscopy was used to investigate the morphology of the MCND support materials compared to three common commercial carbon support materials: Vulcan, KB300 and KB600. From scanning electron microscopy (SEM, Fig. 1a–f and S2†) and transmission electron microscopy (TEM, Fig. S3†) it is apparent that the commercial carbon supports consist of smaller spherical nanoparticles of 30–50 nm, which agglomerate to form small carbon clusters, whereas the MCND materials have larger particles with dendritic shapes. The MCND particles also exhibit a very open 3D-net structure revealing dendritic rods with a width of 50 to 100 nm and length of a few hundred nm. These dendrites branch every 100–200 nm and thus display sufficient space in between, creating a hierarchical structure, which is expected to allow good gas transport if used as electrode materials.

To further investigate the surface area and porosity of the carbons, N_2 physisorption measurements were carried out, with the resulting isotherms presented in Fig. S4.† The pore size distribution for all examined carbon materials is depicted and summarized in Fig. 1h and Table 1, respectively. The pore structure of the carbons was determined through SEM analysis, revealing a slit/cylindrical pore structure, which was used to subsequently select the most appropriate quenched solid density functional theory (QSDFT) model for fitting the pore size distribution of the support materials. The MCND carbon support materials have larger surface areas than the commercial carbons. In particular, MCNDs annealed at 900 and 1200 °C led to sharply larger surface areas, reaching 1731 $m^2\ g^{-1}$ (MCND-900) and 1664 $m^2\ g^{-1}$ (MCND-1200), with a comparable amount of mesopores but slightly fewer micropores for MCND-1200. Increasing the annealing temperature to 1500 °C (MCND-1500) was accompanied by a slightly decreased surface area to 1498 $m^2\ g^{-1}$, mainly due to the reduced amount of micropores compared to MCND-900. The pore size distribution for all three MCND carbon materials was rather narrow with over 63% of mesopores (>2 nm), being between 3 and 5 nm. KB600 showed the highest surface area of all commercial carbons with 1364 $m^2\ g^{-1}$. The pore size distribution of KB600 was less homogeneous compared to the MCND carbons, with pore sizes ranging from 3 to 10 nm in a more asymmetric distribution and only 34% of mesopores being between 3 and 5 nm. KB300 had a significantly lower surface area of around 800 $m^2\ g^{-1}$ with a wide pore size distribution between 2 and 10 nm and 42% of mesopores between 3 and 5 nm. Since Vulcan is considered a solid carbon, compared to the porous carbon Ketjenblack, the surface area is the smallest with just 230 $m^2\ g^{-1}$. The elemental analysis of the carbon species (Table S1†) revealed a small difference in the oxygen content on comparing the commercial carbon supports with 1.1–1.9% oxygen and the MCND materials with 2.3–2.8% oxygen, which is attributed to the nitric acid washing of the pristine MCND material before the annealing step. MCND-900 has the highest amount of oxygen as expected (higher annealing temperatures usually result in a decrease in the oxygen content). The higher amount of oxygen and the high surface area of the MCND carbons could lead to higher carbon corrosion of the material due to an increase in defects inside the material; an increase in graphitization of the carbon could counteract this effect and stabilize the carbon under corrosive conditions.

To investigate the graphitization level of the carbons, Raman spectroscopy was performed statistically on all six samples and pristine MCNDs, the unannealed base material. Normalized average Raman spectra are shown in Fig. S5.† By plotting the intensity ratio between the D (~1350 cm^{-1}) and the G peak (~1580 cm^{-1}) *vs.* the FWHM of the 2D peak (~2700 cm^{-1}) as shown in Fig. 1i, the degree of structural order of different carbon materials, even the bulk material, can be gauged and compared.[26–28] With increasing annealing temperature, the FWHM of the 2D peak, indicative of the degree and kind of stacking order of MCND-900, MCND-1200 and MCND-1500 does not vary significantly, while at the same time, the corresponding I_D/I_G ratio is increasing toward MCND-1500. These trends indicate increasing transformation of amorphous sp^2- and sp^3-bonded carbon atoms into more sp^2 graphitic stacking structures.[29] On the other hand, Vulcan, an oil-furnace black,[3] showed the lowest degree of stacking order and graphitization,[30,31] while KB600 showed an intermediate level of graphitization similar to KB300. The physicochemical characterization of the MCND materials, in particular their pronounced mesoporosity, suggests that they are suitable support materials

Table 1 Results of the surface characterization of the carbon support materials from N_2 physisorption measurements in terms of surface area (BET SA, Brunauer–Emmett–Teller) and pore size distribution using QSDFT analysis

		QSDFT surface area ($m^2\ g^{-1}$)			
Carbon material	BET SA ($m^2\ g^{-1}$)	<2 nm	2–33 nm	Total	Micro/total ratio
Vulcan	229	84	144	228	0.37
KB300	791	273	417	690	0.40
KB600	1364	303	885	1188	0.26
MCND-900	1731	620	890	1510	0.41
MCND-1200	1664	464	883	1347	0.34
MCND-1500	1498	439	845	1284	0.34

with so-called accessible pores for deposition of Pt nanoparticles (accessible carbon).

The deposition of Pt nanoparticles on the six different carbon support materials involved two steps: wet impregnation and reduction under a H_2 atmosphere in a self-engineered fluidized bed reactor (FBR).[32,33] This synthesis method benefits the formation of small and uniform Pt particles distributed well on the carbons. The Pt loading of the catalysts was aimed at 20 wt% (Table S2†). Representative TEM images of all six systems are given in Fig. 2 to support this. The spherically shaped Pt nanoparticles are well distributed across the carbon supports in all samples and have a narrow size distribution between 2 and 3 nm. To assess whether the Pt nanoparticles are located inside the pores of the MCND materials, stereoscopic TEM images were obtained of Pt/Vulcan (Fig. S6†) and Pt/MCND-1500 (Fig. S7†). Two TEM images of the same sample spot were obtained at different specimen angles; by cross-viewing both images or using 3D red cyan glasses for the anaglyph image, the Pt nanoparticle placement on the carbon material can be observed. On Vulcan, as a solid carbon, the Pt nanoparticles are located on the outside of the carbon particles, either on the front or the back. For Pt/MCND-1500, some catalyst nanoparticles are also deposited on the outside of the carbon, but a significant amount is placed inside the pore structure.

XRD measurements were carried out for all six carbon supports with (Fig. S8b†) and without Pt nanoparticles (Fig. S8a†). Two peaks appearing near 26° and 43°, corresponding to the characteristic (002) and (100) planes of carbon, respectively, can be identified for carbon support materials. The (002) peak is attributed to the disordered carbonaceous interlayer, while the (100) peak is related to the crystalline carbon.[34] The (100) diffraction peaks were observed in all carbon supports, while the (002) peak is not present for the MCND carbon materials, indicating fewer structural defects. The samples with deposited Pt nanoparticles all show the diffraction pattern of a Pt face-centered cubic (fcc) structure.

To preliminarily investigate the electrocatalytic ORR properties of the prepared catalysts, RDE measurements were conducted in acidic media. After activation, linear sweep voltammetry (LSV) (Fig. 3a) was conducted in oxygen-saturated electrolyte (0.1 M $HClO_4$) and shows polarization curves for all six catalysts, with Pt/KB300 and Pt/KB600 having the highest halfwave potential, and both Pt/MCND-1500 and Pt/MCND-1200 show smaller geometric activities compared to the other catalysts. The cyclic voltammograms (CVs) (Fig. 3b) are used to determine the electrochemical surface area ($ECSA_{Hupd}$) of the catalysts shown in Fig. 3c. Pt/KB300, Pt/KB600 and Pt/MCND-1500 showed very high ECSA (>120 m^2 g_{Pt}^{-1}). The mass activity (MA) at 0.9 V is determined from the LSVs and depicted in Fig. 3c. Pt/KB300 showed the highest MA with >0.4 A mg_{Pt}^{-1}, while Pt/Vulcan, Pt/KB600 and Pt/MCND-900 also showed similar MA at 0.3–0.4 A mg_{Pt}^{-1}. The RDE results suggested that the new MCND support materials did not perform similarly to the commercial carbons in terms of ECSA and MA, yet showed the beneficial mesoporous accessibility to Pt nanoparticles. Since activity trends in the RDE do not always translate into the fuel cell, further investigations into the performance under fuel cell operating conditions were conducted by MEA single cell measurements (details given in the ESI†).[32]

Fig. 4a shows the beginning of life (BOL) performance of the six different catalysts. The MCND-based Pt catalysts

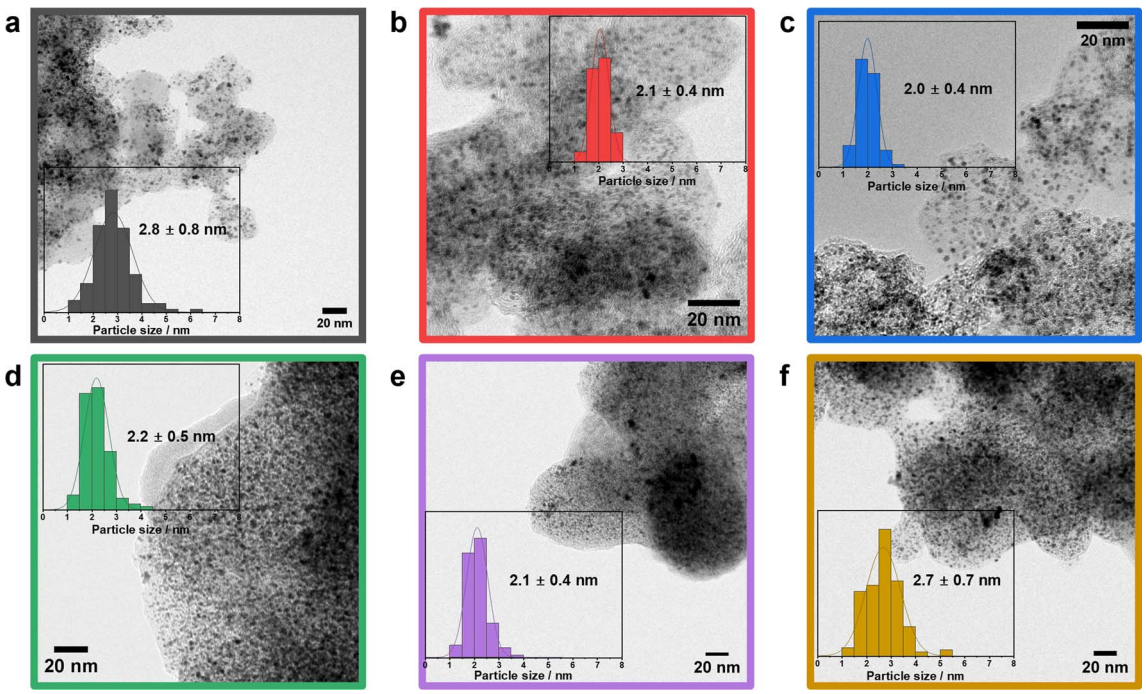

Fig. 2 TEM images and particle size distribution measured for at least 130 particles of the six Pt nanocatalysts supported on (a) Vulcan (black), (b) KB300 (red), (c) KB600 (blue), (d) MCND-900 (green), (e) MCND-1200 (purple), and (f) MCND-1500 (gold).

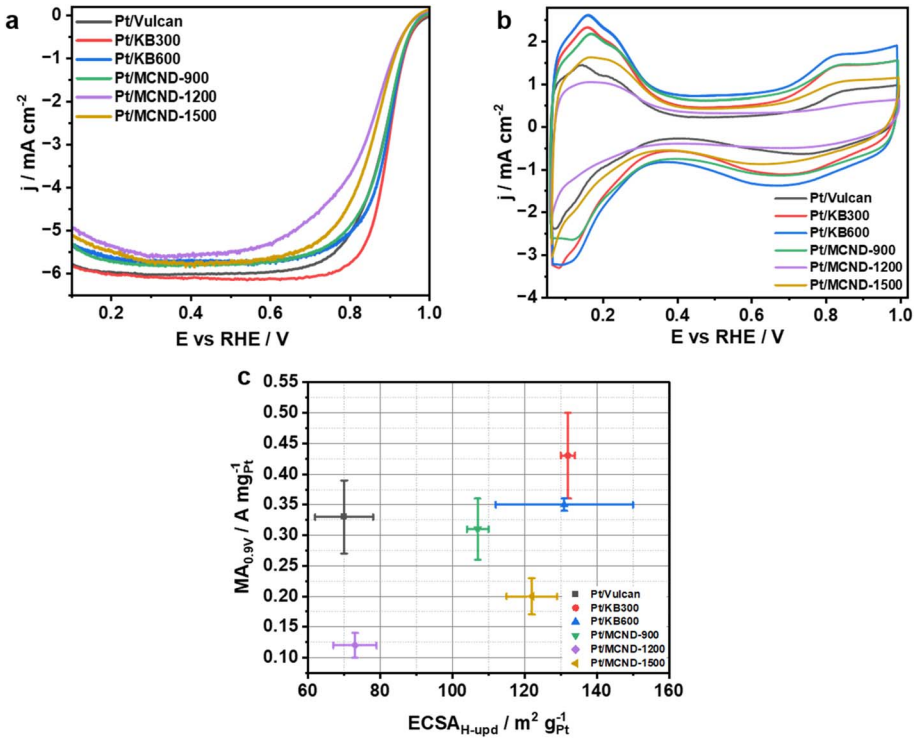

Fig. 3 Electrochemical response curve of (a) LSV and (b) CV. Evolution of the electrochemical parameters in terms of (c) ECSA and ORR mass activity (MA) for Pt/Vulcan (black), Pt/KB300 (red), Pt/KB600 (blue), Pt/MCND-900 (green), Pt/MCND-1200 (purple) and Pt/MCND-1500 (gold) after activation.

outperformed all other commercial systems studied in this work in all current density ranges. This significant improvement translated to a power density increase measured at 1 A cm^{-2} of 6% and 12% between Pt/KB300 and Pt/MCND-900 and Pt/Vulcan and Pt/MCND-1500, respectively. The performance increase is attributable to the improved pore structure of the MCND materials. Accessible pores, as present for these supports, show beneficial kinetic and mass transport properties. Yarlagadda *et al.* proved that the oxygen transport resistance of Pt catalysts within accessible pores is comparable to those on solid carbons.[15] Furthermore, recent studies showed that mesoporous carbons can act as support materials with higher kinetic activity and improved accessibility to protons and oxygen.[16,24,25]

Furthermore, the ECSA in MEA slightly changed compared to RDE data (Fig. S9†) and increased for the MCND-based systems and Pt/Vulcan. The BOL performance of the six catalysts evidenced that the new MCND support material represents a promising alternative to today's most popular support materials. Our results suggest that the beneficial surface area and the tailored accessible pore structure indeed lead to increased performance under relevant fuel cell operating conditions.

The catalysts were then subjected to the harshest Department of Energy (DoE)-recommended AST, tailored to investigate the carbon support materials using high voltage cyclic voltammetry (1–1.5 V; 5k cycles).[35] This protocol was developed to simulate start–stop processes in PEMFCs, but the harsh conditions lead to severe carbon corrosion independently of the carbon support material which is undesirable for the longevity of fuel cell applications. Therefore, mitigation strategies emerged such as dummy loads and gas purges to prevent high voltages and significantly reduce the carbon corrosion in the catalyst layer.[36–38] Borup *et al.* investigated the cells of two Toyota Mirai fuel cell electric vehicles after 300 and 3000 h of real-world driving and found no significant changes between the two catalyst layers.[39] Only after subjecting them to the DOE-recommended catalyst (30 000 square wave voltammograms; 0.6–0.95 V; 3 s dwell time) and carbon support protocols, the catalyst layer showed severe degradation especially a thinning of the layer after the support AST. These results suggest that the mitigation strategies of modern fuel cell systems can inhibit the degradation of the catalyst layer. Furthermore, support materials with high surface areas and thus more exposed surface carbon suffer more from corroding conditions compared to solid carbons. While the conditions of the carbon support AST may not be translatable into real fuel cell applications or accurately predict the durability of real life PEMFCs, the AST can give insight into the degradation mechanism occurring at high voltage cycling and contribute to improving carbon support materials. The cell voltage trajectories during the AST are displayed in Fig. 4b at 0.6 A cm^{-2} over the first 1000 cycles. Pt/Vulcan showed a steady voltage drop over 1k cycles. While having the lowest starting potential at BOL, the catalyst's durability outperformed that of other catalysts. Pt/KB600 and

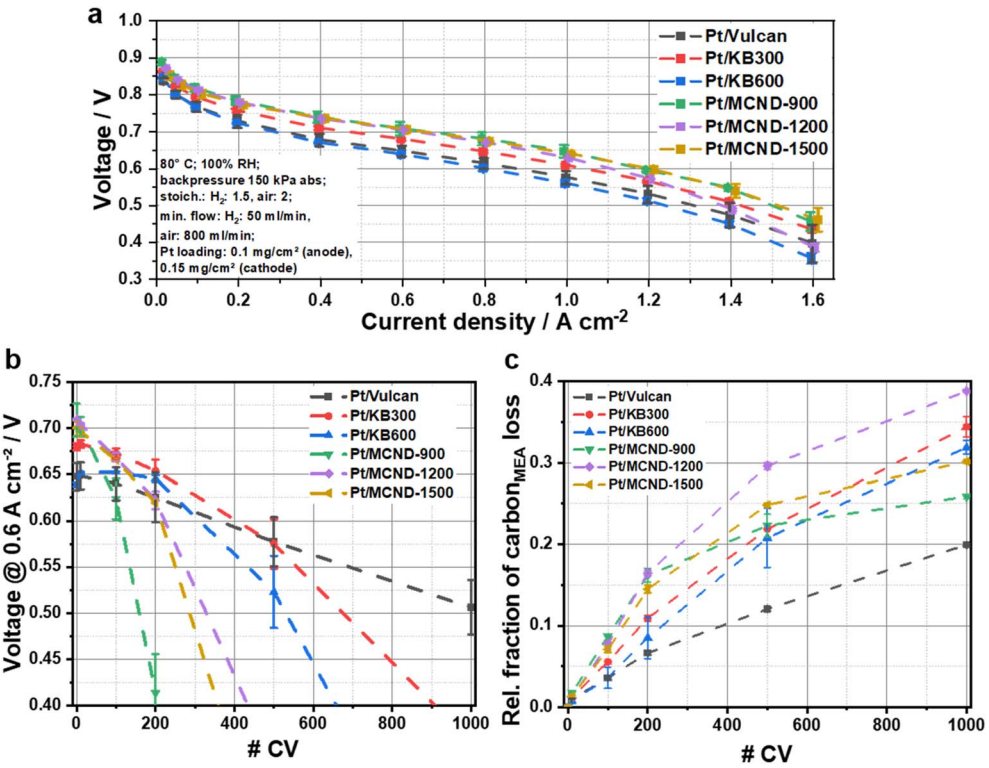

Fig. 4 Fuel cell performance of Pt/V (black), Pt/KB300 (red), Pt/KB600 (blue), Pt/MCND-900 (green), Pt/MCND-1200 (violet), and Pt/MCND-1500 (gold) under operation conditions; (a) BOL polarization curve of 10 cm^2 MEA; (b) evolution of voltage at 0.6 A cm^{-2} during support degradation AST; (c) relative fraction of $carbon_{MEA}$ loss as determined *via* nondispersive infrared (NDIR) measurements during support degradation AST.

Pt/KB300 displayed a steady potential drop over the first 200 cycles, followed by sharp degradation compared to Pt/Vulcan.

The BOL cell voltages of the three MCND-based Pt catalysts were very high with their cycle degradation being more severe than that of the commercial carbon supports. Pt/MCND-900 showed the sharpest potential drop and lost performance after 200 CVs. This can be explained by a partial collapse of the catalyst layer due to severe carbon corrosion. Pt/MCND-1200 and Pt/MCND-1500 featured similar degradation behaviors. The AST confirms that, while the initial performance of the new support materials can outclass those of the commercial carbon, the higher surface area makes these catalysts more vulnerable to carbon corrosion during high potential cycling and the highly porous structure easily susceptible to the collapse of the catalyst layer. This calls for structural collapse mitigation strategies such as higher graphitization or chemical scaffolding using dopants. However, the significantly improved cell performance under regular operation conditions outweighs and is more relevant than AST durability under high potential cycling, because modern cell potential control during fuel cell operations will effectively prevent high voltage excursions and prevent carbon corrosion.

In order to learn more about the degradation mechanism, the cathode exhaust stream was spectroscopically analyzed using a non-dispersive infrared (NDIR) system to detect CO and CO_2 evolving during the AST. This analysis was to confirm that the degradation was related to the corrosion of the carbon supports. Fig. 4c displays the degradation behavior of the different support materials. The detected concentrations of CO and CO_2 in the cathode exhaust stream were integrated and converted to a mass of carbon and divided by the amount of carbon of the catalyst support material. This relative fraction of $carbon_{MEA}$ loss is depicted in Fig. 4c against the number of CVs. This measure was chosen to compare the different carbon materials, which have slightly different Pt-loadings on the carbon supports (Table S2†) leading to different amounts of carbon in the catalyst layer while maintaining the same geometrical Pt loading of 0.15 mg_{Pt} cm^{-2} for the MEAs. Furthermore, neither the carbon from the ionomer nor from the GDL is considered in this calculation due to the difference in the surrounding of the carbon atoms in these cases and therefore different proneness to carbon corrosion. Pt/Vulcan has a slow and steady carbon loss during the first 1000 cycles, showing the most favorable carbon corrosion behavior of the tested catalyst systems. Both KB-based catalysts showed comparable carbon corrosion, being slightly higher than Pt/Vulcan. For the three MCND based catalysts, the carbon corrosion was comparable over the first 200 CVs. Afterwards, Pt/MCND-900 reached a plateau, when no further significant performance was observable. This confirms the collapse hypothesis of the catalyst layer, because large portions of the Pt nanoparticles and the carbon support material were no longer

electrochemically available after this point. This can also be surmised for Pt/MCND-1200 and Pt/MCND-1500 at later stages of the AST. Hence, our single cell MEA measurements indicate that under electronic cell potential control the new MCND "accessible" support material offers excellent potential for sustained high performance fuel cell catalysts due to its unparalleled BOL performance. Meanwhile, the carbon corrosion behavior and therefore the durability of MCND carbons need further attention in order to compete with commercial carbon support materials under extreme voltage cycling conditions.

Conclusion

We have introduced and characterized MCNDs as a new mesoporous carbon material for PEMFC electrodes. The surface characterization of the MCND materials revealed a very high surface area and a narrow pore size distribution between 3 and 5 nm. Statistical Raman spectroscopy showed an increasing graphitization with higher annealing temperatures and less structural disorder compared to three commercial carbons (Vulcan, KB300 and KB600). For the platinization process of the support materials, the synthesis *via* an FBR resulted in small (2–3 nm) and homogeneously distributed spherical Pt particles. RDE measurements showed promising ECSA and MA for the MCND based catalysts comparable to commercial carbon materials. In single cell MEA tests, the MCND catalysts outperformed all commercial counterparts, while very high potential fuel cell cycling proved challenging. Online NDIR measurements of CO and CO_2 in the cathode exit confirmed that the performance losses during AST can be attributed to the carbon corrosion of the support material. The results suggest that the new MCND support material is suited for high performance fuel cells, if the potential is held electronically under 1 V to prevent carbon corrosion, something which is the industry standard today. Further increasing the annealing temperature and therefore the graphitization of the catalysts, while retaining the high surface area, should enhance the carbon corrosion behavior of the MCND support.

Data availability

We claim that the data related to the article are present in the manuscript and the ESI.†

Conflicts of interest

The authors declare no conflicts of interest.

Acknowledgements

This project received financial support from the German Federal Ministry of Education and Research (BMBF) through grant 03XP0251 ("KorrZellKat"). We thank Alina Orfanidi for helpful discussions, Juana Krone for the elemental analysis, and Astrid Müller-Klaucke for ICP-OES measurements. We thank Sören Selve and the Zentraleinrichtung Elektronenmikroskopie of Technische Universität Berlin for their support with electron microscopy measurements. LE would like to thank the Israeli Ministry of Science for their support.

References

1 H. A. Gasteiger, S. S. Kocha, B. Sompalli and F. T. Wagner, Activity benchmarks and requirements for Pt, Pt-alloy, and non-Pt oxygen reduction catalysts for PEMFCs, *Appl. Catal., B*, 2005, **56**(1–2), 9–35, DOI: **10.1016/j.apcatb.2004.06.021**.

2 S. S. Kocha, Polymer Electrolyte Membrane (PEM) Fuel Cells, Automotive Applications, in *Fuel Cells: Selected Entries from the Encyclopedia of Sustainability Science and Technology*, ed. K.-D. Kreuer, Springer, New York, 2013, pp. 473–518.

3 E. Antolini, Carbon supports for low-temperature fuel cell catalysts, *Appl. Catal., B*, 2009, **88**(1–2), 1–24, DOI: **10.1016/j.apcatb.2008.09.030**.

4 A. L. Dicks, The role of carbon in fuel cells, *J. Power Sources*, 2006, **156**(2), 128–141, DOI: **10.1016/j.jpowsour.2006.02.054**.

5 Y. Sun, S. Polani, F. Luo, S. Ott, P. Strasser and F. Dionigi, Advancements in cathode catalyst and cathode layer design for proton exchange membrane fuel cells, *Nat. Commun.*, 2021, **12**(1), 5984, DOI: **10.1038/s41467-021-25911-x**.

6 Y. J. Wang, N. Zhao, B. Fang, H. Li, X. T. Bi and H. Wang, Carbon-supported Pt-based alloy electrocatalysts for the oxygen reduction reaction in polymer electrolyte membrane fuel cells: particle size, shape, and composition manipulation and their impact to activity, *Chem. Rev.*, 2015, **115**(9), 3433–3467, DOI: **10.1021/cr500519c**.

7 Z. Qiao, S. Hwang, X. Li, C. Wang, W. Samarakoon, S. Karakalos, D. Li, M. Chen, Y. He and M. Wang, 3D porous graphitic nanocarbon for enhancing the performance and durability of Pt catalysts: a balance between graphitization and hierarchical porosity, *Energy Environ. Sci.*, 2019, **12**(9), 2830–2841.

8 M. R. Benzigar, S. N. Talapaneni, S. Joseph, K. Ramadass, G. Singh, J. Scaranto, U. Ravon, K. Al-Bahily and A. Vinu, Recent advances in functionalized micro and mesoporous carbon materials: synthesis and applications, *Chem. Soc. Rev.*, 2018, **47**(8), 2680–2721, DOI: **10.1039/c7cs00787f**.

9 N. Choudhary, S. Hwang and W. Choi, Carbon Nanomaterials: A Review, in *Handbook of Nanomaterials Properties*, 2014, pp. 709–769.

10 C. Liang, Z. Li and S. Dai, Mesoporous carbon materials: synthesis and modification, *Angew. Chem., Int. Ed.*, 2008, **47**(20), 3696–3717.

11 M. Liu, R. Zhang and W. Chen, Graphene-supported nanoelectrocatalysts for fuel cells: synthesis, properties, and applications, *Chem. Rev.*, 2014, **114**(10), 5117–5160, DOI: **10.1021/cr400523y**.

12 P. Trogadas, T. F. Fuller and P. Strasser, Carbon as catalyst and support for electrochemical energy conversion, *Carbon*, 2014, **75**, 5–42, DOI: **10.1016/j.carbon.2014.04.005**.

13 K. Shinozaki, Y. Morimoto, B. S. Pivovar and S. S. Kocha, Suppression of oxygen reduction reaction activity on Pt-based electrocatalysts from ionomer incorporation, *J. Power Sources*, 2016, **325**, 745–751.

14 Y. Yang, K. Chiang and N. Burke, Porous carbon-supported catalysts for energy and environmental applications: a short review, *Catal. Today*, 2011, **178**(1), 197–205, DOI: **10.1016/j.cattod.2011.08.028**.

15 V. Yarlagadda, M. K. Carpenter, T. E. Moylan, R. S. Kukreja, R. Koestner, W. Gu, L. Thompson and A. Kongkanand, Boosting Fuel Cell Performance with Accessible Carbon Mesopores, *ACS Energy Lett.*, 2018, **3**(3), 618–621, DOI: **10.1021/acsenergylett.8b00186**.

16 S. Ott, A. Bauer, F. Du, T. A. Dao, M. Klingenhof, A. Orfanidi and P. Strasser, Impact of Carbon Support Meso-Porosity on Mass Transport and Performance of PEMFC Cathode Catalyst Layers, *ChemCatChem*, 2021, **13**(22), 4759–4769, DOI: **10.1002/cctc.202101162**.

17 C. Yu, J. Fan, B. Tian, D. Zhao and G. D. Stucky, High-yield synthesis of periodic mesoporous silica rods and their replication to mesoporous carbon rods, *Adv. Mater.*, 2002, **14**(23), 1742–1745.

18 J. Liu, N. P. Wickramaratne, S. Z. Qiao and M. Jaroniec, Molecular-based design and emerging applications of nanoporous carbon spheres, *Nat. Mater.*, 2015, **14**(8), 763–774.

19 H. Fan, S. Zhou, Q. Wei and X. Hu, Honeycomb-like carbon for electrochemical energy storage and conversion, *Renewable Sustainable Energy Rev.*, 2022, **165**, 112585.

20 Q. Xue, J. B. Huang, D. J. Yang, B. Li and C. M. Zhang, Enhanced PEMFC durability with graphitized carbon black cathode catalyst supports under accelerated stress testing, *RSC Adv.*, 2021, **11**(32), 19417–19425, DOI: **10.1039/d1ra01468d**.

21 X. Tang, Y. Zeng, L. Cao, L. Yang, Z. Wang, D. Fang, Y. Gao, Z. Shao and B. Yi, Anchoring ultrafine Pt nanoparticles on the 3D hierarchical self-assembly of graphene/functionalized carbon black as a highly efficient oxygen reduction catalyst for PEMFCs, *J. Mater. Chem. A*, 2018, **6**(31), 15074–15082, DOI: **10.1039/c8ta02453g**.

22 J. Chen, Z. Ou, H. Chen, S. Song, K. Wang and Y. Wang, Recent developments of nanocarbon based supports for PEMFCs electrocatalysts, *Chin. J. Catal.*, 2021, **42**(8), 1297–1326, DOI: **10.1016/s1872-2067(20)63736-6**.

23 N. Ramaswamy, W. Gu, J. M. Ziegelbauer and S. Kumaraguru, Carbon Support Microstructure Impact on High Current Density Transport Resistances in PEMFC Cathode, *J. Electrochem. Soc.*, 2020, **167**(6), 064515, DOI: **10.1149/1945-7111/ab819c**.

24 G. Wang, W. Zhao, M. Mansoor, Y. Liu, X. Wang, K. Zhang, C. Xiao, Q. Liu, L. Mao, M. Wang and H. Lv, Recent Progress in Using Mesoporous Carbon Materials as Catalyst Support for Proton Exchange Membrane Fuel Cells, *Nanomaterials*, 2023, **13**(21), 2818, DOI: **10.3390/nano13212818**.

25 V. Yarlagadda, N. Ramaswamy, R. S. Kukreja and S. Kumaraguru, Ordered mesoporous carbon supported fuel cell cathode catalyst for improved oxygen transport, *J. Power Sources*, 2022, **532**, 231349, DOI: **10.1016/j.jpowsour.2022.231349**.

26 S. Eigler, Controlled Chemistry Approach to the Oxo-Functionalization of Graphene, *Chemistry*, 2016, **22**(21), 7012–7027, DOI: **10.1002/chem.201600174**.

27 M. M. Lucchese, F. Stavale, E. H. M. Ferreira, C. Vilani, M. V. O. Moutinho, R. B. Capaz, C. A. Achete and A. Jorio, Quantifying ion-induced defects and Raman relaxation length in graphene, *Carbon*, 2010, **48**(5), 1592–1597, DOI: **10.1016/j.carbon.2009.12.057**.

28 A. Sadezky, H. Muckenhuber, H. Grothe, R. Niessner and U. Pöschl, Raman microspectroscopy of soot and related carbonaceous materials: spectral analysis and structural information, *Carbon*, 2005, **43**(8), 1731–1742, DOI: **10.1016/j.carbon.2005.02.018**.

29 D. B. Schuepfer, F. Badaczewski, J. M. Guerra-Castro, D. M. Hofmann, C. Heiliger, B. Smarsly and P. J. Klar, Assessing the structural properties of graphitic and non-graphitic carbons by Raman spectroscopy, *Carbon*, 2020, **161**, 359–372, DOI: **10.1016/j.carbon.2019.12.094**.

30 Y. Holade, C. Morais, K. Servat, T. W. Napporn and K. B. Kokoh, Enhancing the available specific surface area of carbon supports to boost the electroactivity of nanostructured Pt catalysts, *Phys. Chem. Chem. Phys.*, 2014, **16**(46), 25609–25620, DOI: **10.1039/c4cp03851g**.

31 S.-J. Jang, Y. C. Kang, J.-S. Hyun, T. H. Shin, Y. W. Lee and K. C. Roh, Hybrid Structure of TiO_2-Graphitic Carbon as a Support of Pt Nanoparticles for Catalyzing Oxygen Reduction Reaction, *Catalysts*, 2021, **11**(10), 1196, DOI: **10.3390/catal11101196**.

32 E. Hornberger, T. Merzdorf, H. Schmies, J. Hubner, M. Klingenhof, U. Gernert, M. Kroschel, B. Anke, M. Lerch, J. Schmidt, *et al.*, Impact of Carbon N-Doping and Pyridinic-N Content on the Fuel Cell Performance and Durability of Carbon-Supported Pt Nanoparticle Catalysts, *ACS Appl. Mater. Interfaces*, 2022, **14**(16), 18420–18430, DOI: **10.1021/acsami.2c00762**.

33 E. Hornberger, H. Schmies, B. Paul, S. Kühl and P. Strasser, Design and Validation of a Fluidized Bed Catalyst Reduction Reactor for the Synthesis of Well-Dispersed Nanoparticle Ensembles, *J. Electrochem. Soc.*, 2020, **167**(11), 114509, DOI: **10.1149/1945-7111/aba4eb**.

34 W.-J. Lee, S. Bera, C. M. Kim, E.-K. Koh, W.-P. Hong, S.-J. Oh, E. Cho and S.-H. Kwon, Synthesis of highly dispersed Pt nanoparticles into carbon supports by fluidized bed reactor atomic layer deposition to boost PEMFC performance, *NPG Asia Mater.*, 2020, **12**, 40, DOI: **10.1038/s41427-020-0223-x**.

35 Multi-Year Research, Development, and Demonstration Plan - Section 3.4 Fuel Cells, U.S. Department of Energy, 2018, **https://www.energy.gov/sites/prod/files/2017/05/f34/fcto_myrdd_fuel_cells.pdf**, accessed 09.03.2024.

36 M. Gerbec, V. Jovan and J. Petrovčič, Operational and safety analyses of a commercial PEMFC system, *Int. J. Hydrogen Energy*, 2008, **33**(15), 4147–4160, DOI: **10.1016/j.ijhydene.2008.04.063**.

37 Z. Liu, H. Chen and T. Zhang, Review on system mitigation strategies for start-stop degradation of automotive proton

exchange membrane fuel cell, *Appl. Energy*, 2022, **327**, 120058, DOI: **10.1016/j.apenergy.2022.120058**.

38 J. Zhao, Z. Tu and S. H. Chan, Carbon corrosion mechanism and mitigation strategies in a proton exchange membrane fuel cell (PEMFC): a review, *J. Power Sources*, 2021, **488**, 229434, DOI: **10.1016/j.jpowsour.2020.229434**.

39 R. L. Borup, A. Kusoglu, K. C. Neyerlin, R. Mukundan, R. K. Ahluwalia, D. A. Cullen, K. L. More, A. Z. Weber and D. J. Myers, Recent developments in catalyst-related PEM fuel cell durability, *Curr. Opin. Electrochem.*, 2020, **21**, 192–200, DOI: **10.1016/j.coelec.2020.02.007**.